

Ionic modulation and ionic coupling effects in MoS₂ devices for neuromorphic computing

Xiaojian Zhu¹, Da Li², Xiaogan Liang ¹ and Wei D. Lu ¹

Coupled ionic-electronic effects present intriguing opportunities for device and circuit development. In particular, layered two-dimensional materials such as MoS₂ offer highly anisotropic ionic transport properties, facilitating controlled ion migration and efficient ionic coupling among devices. Here, we report reversible modulation of MoS₂ films that is consistent with local 2H-1T′ phase transitions by controlling the migration of Li⁺ ions with an electric field, where an increase/decrease in the local Li⁺ ion concentration leads to the transition between the 2H (semiconductor) and 1T′ (metal) phases. The resulting devices show excellent memristive behaviour and can be directly coupled with each other through local ionic exchange, naturally leading to synaptic competition and synaptic cooperation effects observed in biology. These results demonstrate the potential of direct modulation of two-dimensional materials through field-driven ionic processes, and can lead to future electronic and energy devices based on coupled ionic-electronic effects and biorealistic implementation of artificial neural networks.

ransition-metal dichalcogenides (TMDs) have attracted significant interest as promising candidates for future electronic¹, optoelectronic² and valleytronic³ device applications, with highly anisotropic electrical and ionic transport characteristics in the in-plane and the out-of-plane directions⁴⁻⁶ due to their layered crystal structures. Furthermore, TMDs exhibit different polymorphs (structural phases) that offer distinct physical properties7. For example, MoS₂ in the 2H phase with a trigonal prismatic structure is semiconducting, and becomes metallic when it is converted to the 1T (1T') phase with a (distorted) octahedral structure⁸⁻¹⁰. Multiple structural phases can coexist in a single TMD film (for example, 2H and 1T' phases in MoS₂ (ref. 11) and MoTe₂ (ref. 12), making it possible to construct devices whose functions are determined solely by the structural phase configurations¹¹⁻¹⁵. Several approaches, such as chemical¹¹ and electrostatic¹⁶ doping, laser¹²/ electron¹³ irradiation and thermal annealing¹⁷, have so far been shown to induce $2H \rightarrow 1T(1T')$ or $1T(1T') \rightarrow 2H$ phase transitions in TMDs. However, reversible, local phase transitions that can be controlled in situ, by an applied electric field, have not been realized.

Here, we report direct modulation of layered MoS₂ films that is consistent with reversible 2H–1T′ phase transitions, through electric field-controlled Li⁺ ion migration in the in-plane direction. Devices based on this effect show reliable memristive behaviours, where the local high (low) Li⁺ ion concentration promotes transition to the metallic 1T′ phase (semiconducting 2H phase), respectively. The high in-plane mobility of Li⁺ ions further allows multiple devices to be efficiently coupled through ionic exchange in a biorealistic fashion. Synaptic competition and synaptic cooperation behaviours, important for the stabilization and operation of biological networks, can be naturally implemented among multiple coplanar devices.

Natural MoS₂ exists predominately in the 2H phase^{7,9}. A multi-layered 2H-MoS₂ film with a large interlayer spacing (0.62 nm) can accommodate reversible storage and release of Li⁺ ions¹⁸ that can lead to the 2H \rightarrow 1T' structural phase transition⁸, possibly due to electron transfer from the intercalated Li atoms to the Mo 4d orbitals that destabilizes the 2H-MoS₂ crystal structure¹⁰. Previous studies^{18–20}

also show that Li⁺ ions in MoS₂ films have a high in-plane diffusivity. These results led us to hypothesize that Li⁺ ion migration in MoS₂, driven by an applied electric field, can cause reversible structural phase transitions. Specifically, in a lithiated 1T'-MoS₂ film (Fig. 1a), an electric field can drive the in-plane migration of Li⁺ ions and modify the local Li concentration (highlighted box area in Fig. 1a), leading to localized structural phase transitions that are reflected as memristive effects in the MoS₂ devices.

We start with a planar structured Au/Li_xMoS₂ (~40 nm thick)/Au device intercalated with a high concentration of Li⁺ ions (Methods). The presence of Li in the lithiated films was confirmed by X-ray photoelectron spectroscopy (XPS) measurements (Supplementary Fig. 1). Furthermore, Mo⁴⁺ ions in the MoS₂ film were found to be partially reduced to Mo³⁺ after lithiation (Fig. 1b). The conversion to the 1T' phase in the lithiated film was verified by the appearance of the characteristic Raman bands of 1T'-MoS₂ (200, 225 and 355 cm⁻¹)²¹⁻²³ (Fig. 1c). The Raman mapping results indicate that Li intercalation starts from film edges, as the edge regions show a higher concentration of 1T' phase than the interior regions²³ (Supplementary Fig. 2).

Following the lithiation process, current-voltage (I-V) measurements showed that the device conductance (measured at $0.3\,\mathrm{V}$) was increased by $\sim 10^3 \times$ compared with the same device in the 2H phase, and the nonlinear and asymmetric I-V curve observed in the original device became linear and symmetric after lithiation (Supplementary Fig. 3), in agreement with the formation of the metallic $1\mathrm{T'}$ phase and the conversion of Schottky contacts to Ohmic contacts at the $\mathrm{Au/Li_xMoS_2}$ interfaces. Increasing the lithiation time leads to an increase in the $\mathrm{Mo^{3+}}$ ion fraction in the films and the device conductance (Supplementary Fig. 4), indicating that the $\mathrm{Li^+}$ ions intercalated in the $\mathrm{MoS_2}$ film are causing the metallic $1\mathrm{T'}$ phase formation.

The device behaviour was then studied by controlling the voltage bias on the electrodes, which produces in-plane electric fields in the Li_xMoS₂ film. After applying a negative voltage scan (0 V \rightarrow –6 V \rightarrow 0 V) on electrode A (with electrode B grounded, Fig. 1a), the device, initially at a low-resistance state (LRS), was gradually switched

¹Department of Electrical Engineering and Computer Science, The University of Michigan, Ann Arbor, MI, USA. ²Department of Mechanical Engineering, The University of Michigan, Ann Arbor, MI, USA. *e-mail: wluee@umich.edu

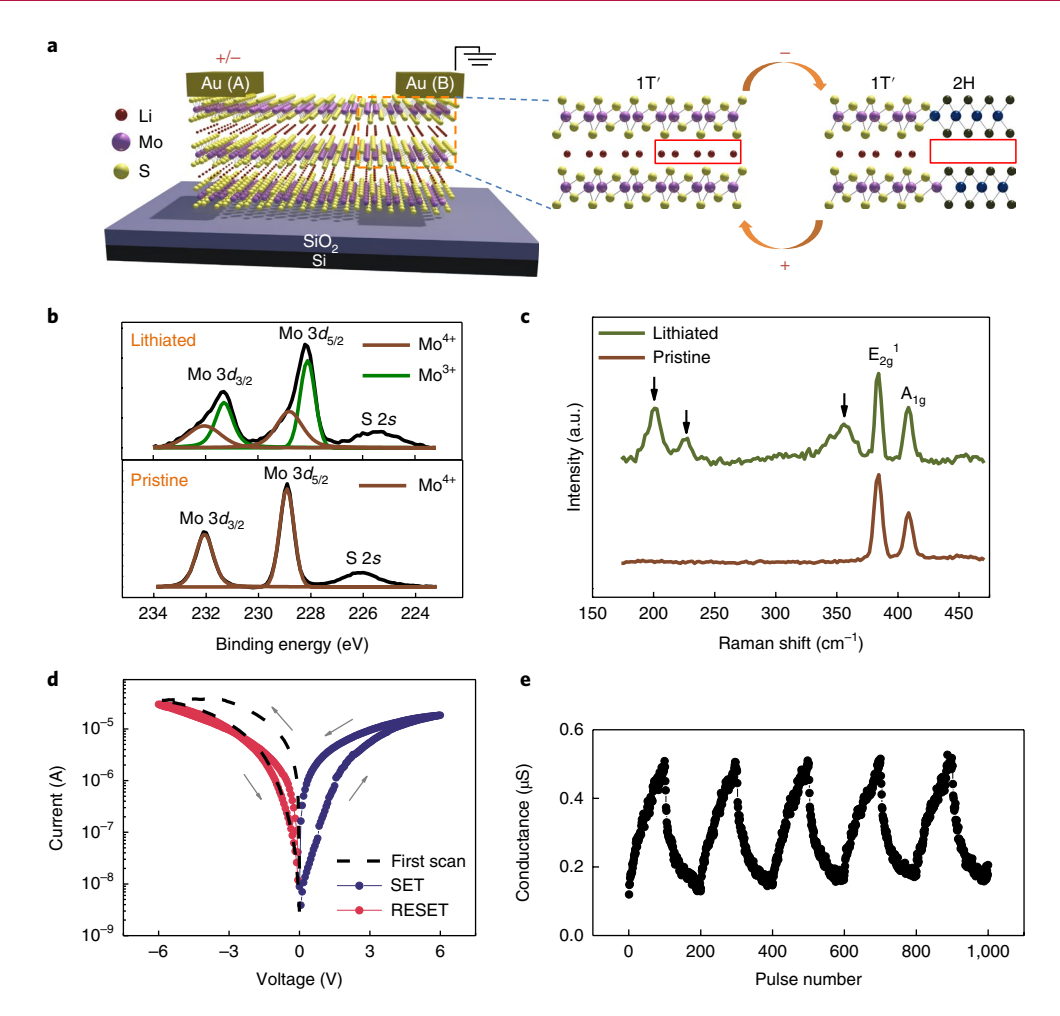


Fig. 1| Electric field control of reversible 2H-1T' phase transition in Li_xMoS₂ films. a, A schematic showing local 2H-1T' phase transitions in Li_xMoS₂ through controlled Li⁺ ion migration, where an increase (decrease) in the Li⁺ ion concentration induces the 1T' (2H) MoS₂ phase. In our studies, one of the electrode (electrode B) is normally grounded, and voltage bias is applied on the other electrode (electrode A) to drive Li⁺ ion migration in the Li_xMoS₂ films. **b**, XPS spectra for the lithiated (top) and pristine (bottom) MoS₂ films. For the lithiated film, the measured data (black) can be deconvolved into the characteristic Mo⁴⁺ peaks located at 228.8 eV (Mo⁴⁺ $3d_{5/2}$) and 232.1 eV (Mo⁴⁺ $3d_{3/2}$) as well as Mo³⁺ peaks located at 228.1 eV (Mo³⁺ $3d_{5/2}$) and 231.3 eV (Mo³⁺ $3d_{3/2}$). The fraction of Li⁺ ions in the Li_xMoS₂ film was estimated to be ~65.0% from the Mo³⁺ fraction. Only the characteristic Mo⁴⁺ peaks were observed for the pristine film. **c**, The Raman spectra collected from lithiated and pristine MoS₂ films. The in-plane E_{2g} peak (384 cm⁻¹) and out-of-plane A_{1g} peak (404 cm⁻¹) of MoS₂ were observed in both samples. Additional peaks located at 200, 225 and 355 cm⁻¹ (marked by the arrows), corresponding to the characteristic Raman peaks of 1T'-MoS₂, were observed in the lithiated film. **d**, Typical *I-V* characteristics of a Au/Li_xMoS₂/Au device. The black dashed line corresponds to the first switching process from the LRS to the HRS. Afterwards, the device can be SET to the LRS and RESET to the HRS with voltage sweeps. **e**, Incremental conductance changes through pulse programming. The device was programmed by 100 positive pulses (4 V, 1 ms) followed by 100 negative pulses (-4 V, 1 ms). The sequence was repeated five times. The conductance was measured by a read pulse (0.3 V, 1 ms) after each programming pulse.

to a high-resistance state (HRS) with an approximately $40\times$ reduction in conductance (black dashed curve in Fig. 1d). Afterwards, the device can be alternately switched to the LRS (termed the SET process, blue curve in Fig. 1d) and the HRS (termed the RESET process, red curve in Fig. 1d) with a ~50× increase and decrease in conductance, by applying positive and negative voltages on electrode A, respectively. The HRS is also accompanied by a rectified I-V behaviour showing a lower current at positive bias, suggesting Schottky contact at the electrode/MoS₂ interface. These results are consistent with the hypothesis schematically shown in Fig. 1a, where a negative (positive) voltage applied on electrode A attracts (repels) the Li⁺ ions towards (from) electrode A and reduces (increases) the Li⁺ ion concentration near electrode B. The depletion (accumulation) of Li⁺ ions will cause the Li_xMoS₂ to convert to the semiconducting 2H (metallic 1T') phase, thus leading to the formation of

Schottky (Ohmic) contact at the electrode-B/Li_xMoS₂ interface and the observed resistive switching effects (Supplementary Fig. 5). The conduction behaviour at the LRS can be fitted by the Mott variable range hopping model (Supplementary Fig. 6), consistent with previous studies²⁴ on MoS₂ films with hybrid 2H/1T' phases, where electron transport is through hopping between local 1T' phase islands surrounded by the 2H phase film. Furthermore, the device conductance can be incrementally increased and decreased through the application of short voltage pulses (for example, ±4 V, 1 ms) (Fig. 1e), allowing the device to emulate synaptic potentiation/depression behaviours²⁵. Good endurance and retention can also be obtained (Supplementary Figs. 7 and 8), verifying the device's potential for neuromorphic computing applications.

A number of control experiments were performed to verify the role of Li⁺ ions in the observed memristive effects. For example,

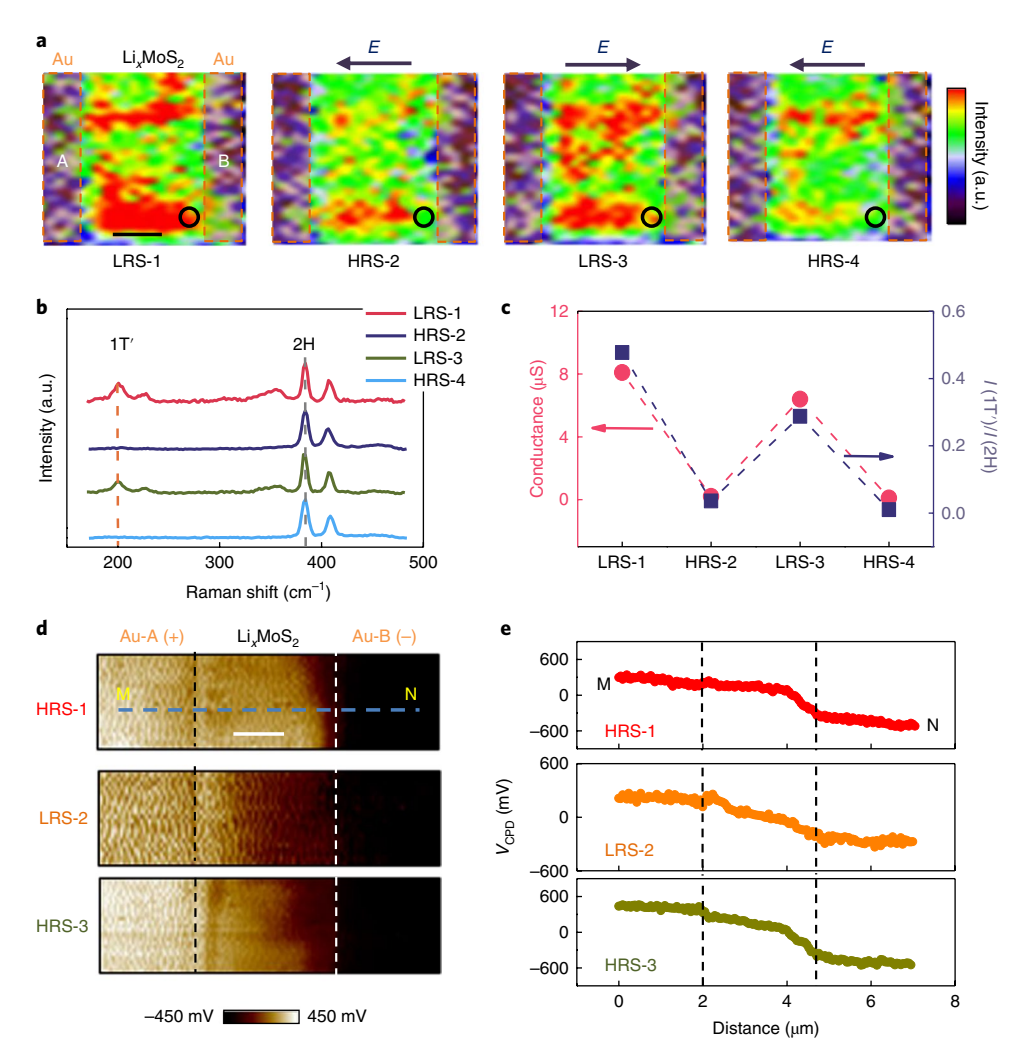


Fig. 2 | 2H/1T′ phase composition tuning in Li_xMoS₂. **a**, Raman intensity maps showing the evolution of the 1T′-MoS₂ phase concentration in a device switched between the LRS (LRS-1 and LRS-3) and the HRS (HRS-2 and HRS-4). The Raman intensity values were obtained by integrating signals in the range of 180-230 cm⁻¹ that covers the characteristic Raman modes of 1T′-MoS₂ at 200 and 225 cm⁻¹. The dashed lines outline the electrode regions. The arrow above each map indicates the applied electric field direction used to program the device. Scale bar, 2 μm. **b**, Raman spectra collected at the marker (open circle) position in **a**. The vertical orange and grey dashed lines mark the positions of the characteristic Raman mode of 1T′-MoS₂ (200 cm⁻¹) and 2H-MoS₂ (384 cm⁻¹), respectively. The spectra were normalized against the intensity of the Raman mode at 384 cm⁻¹. **c**, Correlation of device conductance changes with the 1T′/2H phase Raman intensity ratio (measured at the marked region near electrode B from **b**) during resistive switching processes. **d**, KPFM images showing surface potential distributions in a device after being programmed to different resistance states. State HRS-1 was obtained by applying a negative voltage on electrode A (with electrode B grounded). A positive voltage applied on electrode A switched the device to state LRS-2. Afterwards, the device was switched to state HRS-3 by applying a negative voltage on electrode A again. The KPFM measurements were performed with a bias voltage of -1V across the device. Scale bar, 1 μm. **e**, Surface potential profiles along line MN (marked in **d**) in the device, at different resistance states.

memristive effects were not observed in control samples without lithiation, for voltage ranges up to $\pm 10\,\mathrm{V}$ (Supplementary Fig. 9), while increasing the original lithiation time leads to an increased on/off ratio of the device during resistive switching processes (Supplementary Fig. 10). Furthermore, after removing Li⁺ ions from the lithiated MoS₂ films through deionized water treatment²⁶, the memristive effects disappeared again (Supplementary Fig. 11). These results support the hypothesis that the observed memristive effects are driven by electric field-controlled Li⁺ ion migration.

In situ Raman mapping measurements were then performed to verify the possibility of Li⁺ ion-induced structural phase transitions. Figure 2a shows the Raman intensity maps focusing on the characteristic 1T'-MoS₂ bands in a Au/Li_xMoS₂/Au device at different states during resistive switching processes. For the device at the LRS (for example, state LRS-1 and state LRS-3), a high concentration of the 1T' phase was observed. After applying a negative bias on

electrode A that switched the device to the HRS (for example, state HRS-2 and state HRS-4), the 1T' phase concentration was significantly decreased, particularly in the region close to electrode B (highlighted by the marker), verifying that the 1T' phase concentration in the Li_xMoS₂ film can be reversibly modulated by an electric field²³. Raman spectra collected at the marker position are shown in Fig. 2b, highlighting changes in the 1T' phase concentration at different resistance states. Correlation of the resistance changes and the 2H-1T' phase transitions can be clearly observed in Fig. 2c, which plots the intensity ratio between the Raman peaks at 200 cm⁻¹ (the characteristic peak of 1T' phase²¹⁻²³) and 384 cm⁻¹ (the characteristic peak of 2H phase²⁴), as well as the device conductance during the resistive switching processes. The increase (decrease) in device conductance is accompanied by an increase (decrease) in the 1T'/2H peak intensity ratio, confirming that the memristive effects are correlated with the controlled, local 2H-1T' phase transitions in the Li_xMoS₂ film.

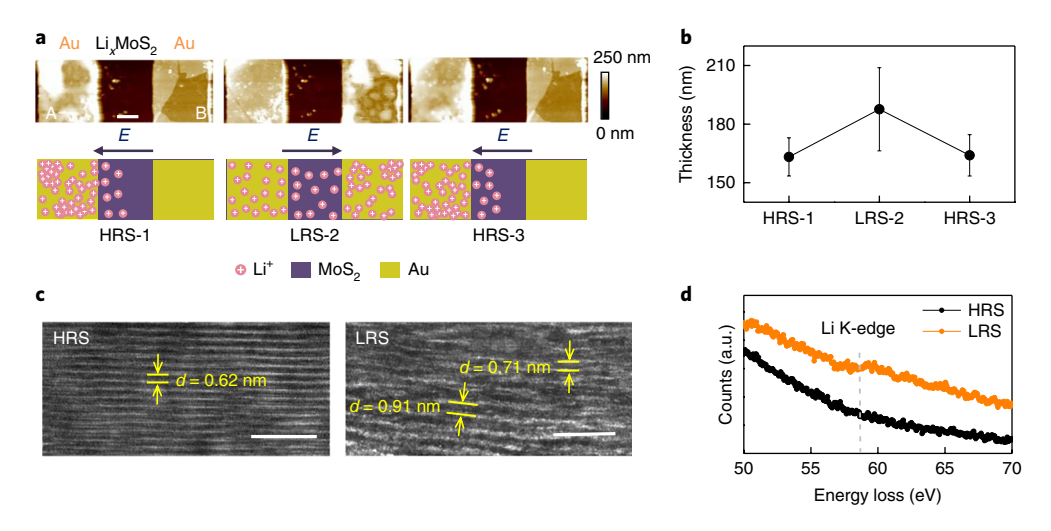


Fig. 3 | Li_xMoS₂ film morphology changes caused by Li⁺ ion redistribution. **a**, AFM height images (top) of a device at different resistance states, and schematics (bottom) showing the corresponding Li⁺ ion distribution. The arrows indicate the applied electric field direction used to program the device. Scale bar, $2 \mu m$. **b**, Thickness of the electrode-B/Li_xMoS₂ film stack at different resistance states, extracted from **a**. The error bars represent the standard deviation of the thickness values obtained at different locations in the sample, measured at each resistance state. Larger film thickness variations are observed at the LRS, consistent with the local 2H-1T' phase transition hypothesis. **c**, Cross-sectional HRTEM images of the Li_xMoS₂ film underneath electrode B in two devices that have been switched to the HRS (left) and LRS (right), respectively. A uniform interlayer spacing of ~0.62 nm is obtained in the HRS sample. In contrast, the interlayer spacing is increased and becomes non-uniform in the LRS sample. Two positions with an interlayer spacing of 0.91 nm and 0.71 nm are marked. Scale bars, 5 nm. **d**, EELS spectra collected from the Li_xMoS₂ film underneath electrode B in two devices that have been switched to the LRS and HRS, respectively. The dashed line marks the position of the Li K-edge at ~58 eV.

Kelvin probe force microscope (KPFM)²⁷ measurement results obtained from a biased Au/Li, MoS2/Au device at different resistance states reveal that the resistance modulation mainly occurs at the electrode-B/Li, MoS, interface (Fig. 2d,e). Specifically, at HRS (for example, state HRS-1 and state HRS-3) most of the potential is dropped at the electrode-B/Li_xMoS₂ film interface, whereas at the LRS (for example, state LRS-2) a uniform drop in potential across the film region between the two electrodes is observed. These results are consistent with the hypothesis that the resistive switching processes are accompanied by the formation/elimination of the Schottky barrier at the electrode-B/Li, MoS, interface, controlled by the Li⁺ ion-induced semiconductor (2H phase) → metal (1T' phase) transitions. This explanation was further supported by direct examination of the MoS, film underneath the electrodes, using transparent Au (5 nm)/ITO (50 nm) electrodes to allow Raman measurements on the MoS₂ film underneath (Supplementary Fig. 12), where reversible tuning of the 1T' phase fraction was observed.

The resistive switching mechanism was further analysed by examining the evolution of the device morphology during the resistive switching processes. Atomic force microscopy (AFM) measurements show that when the device was programmed to the LRS (HRS), the thickness of the electrode-B/Li_xMoS₂ film stack was increased (decreased) (Fig. 3a,b). Similar film thickness changes were also observed in the Li_xMoS₂ film close to electrode B (Supplementary Fig. 13). Figure 3c shows cross-sectional highresolution transmission electron microscopy (HRTEM) images of the Li_xMoS₂ film under electrode B in two devices that have been switched to the HRS and LRS, respectively. Parallel MoS, lattice fringes with a uniform interlayer spacing (~0.62 nm) were observed in the HRS sample, whereas distorted MoS, lattice fringes with a larger and non-uniform interlayer spacing (for example, 0.91 nm and 0.71 nm at the two positions marked in Fig. 3c) were observed in the LRS sample. Careful analysis of the HRTEM image of the LRS sample revealed distorted local lattice structures, consistent with 1T' phase formation at the LRS state (Supplementary Fig. 14). The Li K-edge located at ~58 eV²⁸ collected from the electron energy-loss

spectroscopy (EELS) spectrum is also more pronounced in the LRS sample (Fig. 3d), consistent with Li intercalation that leads to the expansion of the MoS_2 film^{21,29}. These results verify that the resistive switching effects are caused by the field-driven Li⁺ ion redistribution that changes the local Li⁺ ion concentration. Note that, to clearly show the effect of Li intercalation on morphology changes, a constant bias voltage (5 V) for several minutes was used to program the device. Typical operation conditions in our studies are based on the voltage sweep mode, where the morphology change of the device was more moderate (Supplementary Fig. 15).

Interestingly, Fig. 3a shows that when the device was programmed from state HRS-1 to state LRS-2, the morphology changes occurred not only at the left edge of electrode B, but also over the entire electrode region. Since the in-plane electric field under the electrode is probably low, this observation can be explained by the lateral Li⁺ ion diffusion^{20,30} due to the high (in-plane) diffusivity of Li⁺ ions in MoS₂. Specifically, the layered crystal structure of two-dimensional (2D) materials provides ionic pathways with a low activation energy in between the layers^{18–20}, in contrast with other widely studied resistive switching materials (for example, TaO_x (ref. ³¹) and SiO₂ (ref. ³²) having randomly distributed defective sites and a high energy barrier for ion (for example, O²⁻ and Ag⁺) migration.

In the following, we take advantage of the high (in-plane) diffusivity of Li⁺ ions in MoS₂ multilayer films to establish effective ionic coupling that emulates synaptic interactions in biological systems. Synaptic interactions^{33–36}, including synaptic competition and synaptic cooperation³³, are believed to be critical for the stability and functions of the network³⁷. In general, synaptic interactions are induced by the diffusion of plasticity-related proteins (PRPs) (for example, CaMKII, calmodulin-dependent kinase II) that are needed for synaptic growth among adjacent synapses³³ (Fig. 4a). Implementing synaptic interactions will be important for artificial neural networks, including memristor-based neuromorphic systems. However, previous implementations of synaptic interactions were achieved either through circuit concepts aided by software³⁸ or through voltage-divider effects aided by an external voltage

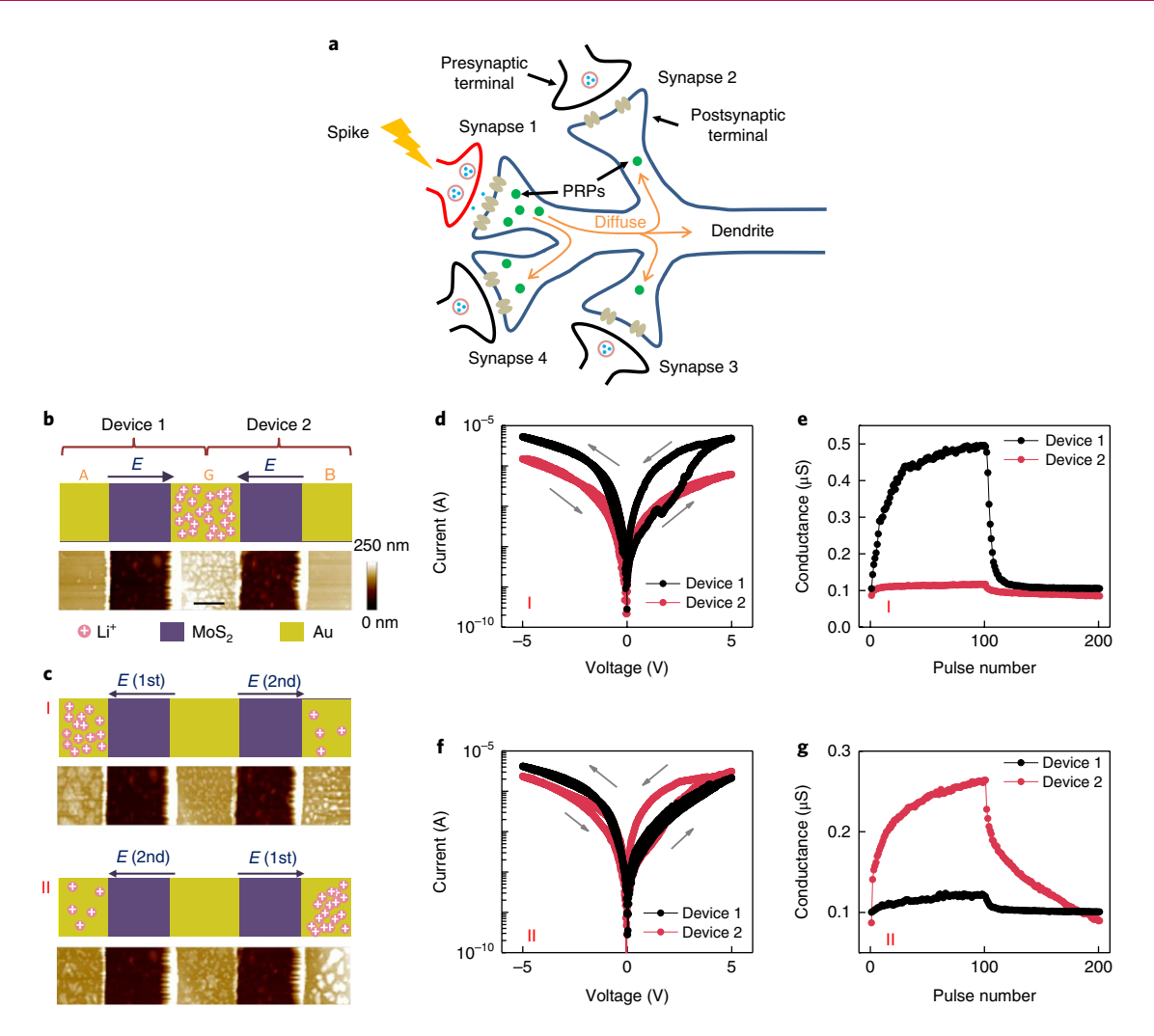


Fig. 4 | Implementation of synaptic competition among Li_xMoS₂ devices. a, A schematic showing synaptic interactions enabled by the diffusion of PRPs among multiple synapses. Specifically, PRPs are generated in the postsynaptic terminal of synapse 1 (stimulated synapse), and can diffuse to the postsynaptic terminals of synapses 2, 3 and 4 (non-stimulated synapses) through the dendrite. If the amount of PRPs is limited, synapses 2 and 3 compete for the limited PRP supply for their development, leading to synaptic competition effects. On the other hand, the diffusion of PRPs to a nearby non-stimulated synapse (for example, synapse 4) can facilitate synaptic potentiation in a cooperative fashion. b,c, Schematics showing the distribution of Li⁺ ions (top), and AFM height images (bottom) of devices 1 and 2 in the initial condition (b), and in configurations I and II (c). The initial condition (b) was created by applying positive bias voltages on both electrodes (with electrode G grounded) to drive Li⁺ ions towards electrode G. Configuration I (c, upper panel) was created by first applying a negative bias voltage on electrode A, followed by a negative bias voltage on electrode B, resulting in more Li⁺ ions accumulated in device 1 compared to those in device 2. Configuration II (c, upper panel) was created through the reverse sequence, resulting in the accumulation of more Li⁺ ions in device 2 compared to those in device 1. Scale bar, 2 μm. d-g, I-V characteristics (d,f) and synaptic potentiation/ depression effects (e,g) of the two devices in configurations I (d,e) and II (f,g). The synaptic potentiation and depression behaviours were tested with 100 positive and 100 negative stimulation pulses, with a pulse amplitude of 6 V and a pulse duration of 1 ms. The device conductance was measured with a read pulse (0.3 V, 1 ms) after each programming pulse.

bias³⁹, rather than through internal processes that directly emulate the synaptic dynamics observed in biology. Ionic coupling between MoS_2 -based memristive devices, which can take place through Li⁺ ion exchange via Li⁺ ion diffusion in the MoS_2 layer, can potentially emulate the PRP exchange processes among biological synapses and enable biorealistic implementation of synaptic competition and synaptic cooperation effects.

Synaptic competition among different memristive devices was attempted first. We note that the amount of Li+ ions available in the Li_xMoS_2 film can be limited (see Supplementary Figs. 16–18 for further experimental results and analysis). Competition for this limited ion supply may thus be used for the implementation of synaptic competition behaviours in analogy to the competition for the limited

PRPs in biological neural networks. Figure 4b,c shows a schematic of synaptic competition between two adjacent devices. Here, two memristive devices are designed to share a common electrode, electrode G, that is normally grounded and resembles the postsynaptic terminals that are connected to a dendrite. The regions at electrodes A and B resemble the presynaptic terminals of the two synapses. Li⁺ ions in devices 1 and 2 were initially driven towards the region under electrode G after an initialization process, emulating the dendrite region where limited PRPs are accumulated (Methods). The system was then conditioned to configuration I through voltage bias (Methods), where device 1 received more Li⁺ ions than device 2 as verified by the thicker electrode-A/Li_xMoS₂ film stack compared with the electrode-B/Li_xMoS₂ film stack (configuration I in

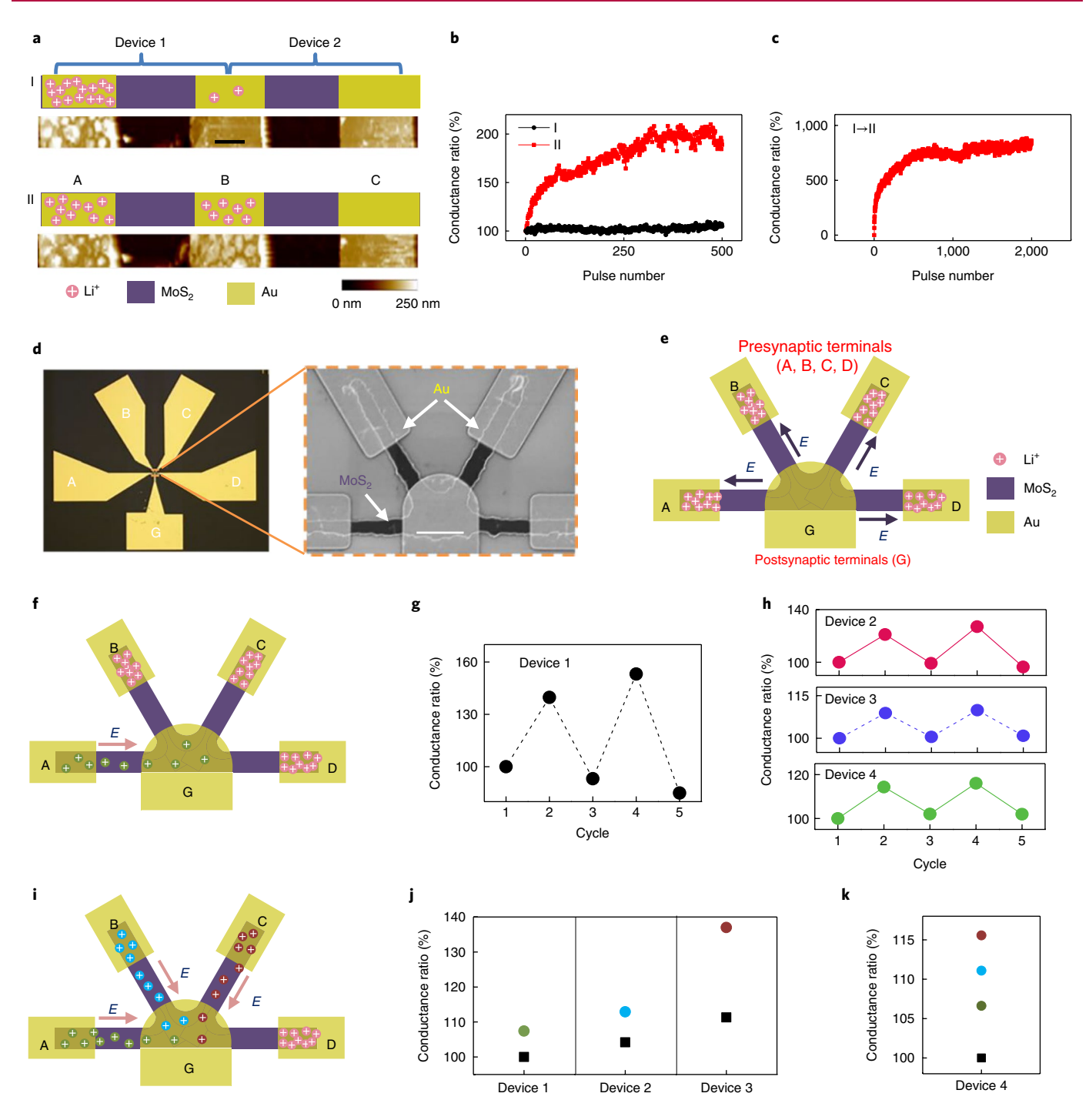


Fig. 5 | Implementation of synaptic cooperation among Li_xMoS₂ devices. a, Schematics of the Li⁺ ion distribution and AFM height images of a system consisting of two devices. Scale bar, 2 μm. Configuration I (top panel) was created by applying –5 V on electrode A for several minutes with electrode C grounded, causing most of the Li⁺ ions in the system to accumulate near electrode A. Configuration II (lower panel) was created afterwards by applying 2,000 stimulation pulses (7 V, 5 ms) on electrode A with electrode B grounded, allowing Li⁺ ions to be accumulated under electrode B. b, Potentiation behaviours of device 2 at the two different configurations, showing no response at configuration I and effective potentiation at configuration II, respectively. c, Evolution of device 1 conductance when the system is changed from configuration I to configuration II. d, Optical (left) and scanning electron (right) micrographs of a network structure consisting of four Li_xMoS₂ devices. Scale bar, 5 μm. e, Schematic of the Li⁺ ion distribution in the network at the initial condition, created by applying negative bias (–4 V) on the four electrodes A, B, C and D, leading to the depletion of Li⁺ ions under electrode G. f, A positive bias on electrode A drove Li⁺ ions towards electrode G and potentiated device 1. g, Potentiation and depression cycles of device 1. h, The corresponding conductance changes in non-stimulated devices 2, 3 and 4 when device 1 was potentiated/depressed. i, Schematic of the Li⁺ ion distribution after successive potentiation of devices 1, 2 and 3, by applying positive bias (4 V) on electrodes A, B and C, respectively. j, Conductance changes in devices 1, 2 and 3, measured before (squares) and after (circles) the successive stimulations of the other three devices.

Fig. 4c). In this case, device 1 (black curves) showed a much stronger memristive effect than device 2 (red curves), as verified by the I-V characteristics shown in Fig. 4d, where a much larger current hysteresis ratio (~10) is obtained for device 1 than that for device 2 (~2.7). Similarly, in pulse-based synaptic potentiation (depression) tests, the degree of potentiation/depression of device 1 was much higher than that of device 2 (Fig. 4e), as indicated by a larger conductance change ratio after pulse stimulation (~500% for device 1 versus ~150% for device 2). On the other hand, if the devices were instead conditioned to configuration II (Methods) so that device 2 received more Li⁺ ions than device 1, device 2 would show stronger memristive effects while the memristive effects in device 1 would be suppressed (Fig. 4f,g). Further studies show that the distribution of Li+ ions among the devices is affected by the amplitude and duration of the voltage bias used to initialize the system (Supplementary Figs. 19 and 20). These results show that increasing the degree of potentiation (depression) in one Li, MoS2-based synaptic device reduces the activity of the other, emulating the synaptic competition behaviour in biological networks. The competitive processes can be repeated for at least 25 cycles between 2 Li_xMoS₂ synaptic devices without obvious degradation (Supplementary Fig. 21), suggesting that practical implementation of synaptic competition may be feasible with further device and programming parameter optimizations.

Synaptic cooperation effects are also verified in Li_xMoS₂ devices, as shown in Fig. 5. We first show that the potentiation of one synaptic device can be facilitated by the potentiation of a neighbouring synaptic device. Here, devices 1 and 2 were first initialized to configuration I (Methods), where Li+ions in the two devices were accumulated under electrode A (Fig. 5a). When attempting to potentiate device 2 with 500 stimulation pulses (6 V, 1 ms) (Methods), no obvious potentiation effect (conductance increase) was observed (black curve in Fig. 5b). On the contrary, after a new condition, configuration II, was established by applying strong stimulation pulses to device 1 (2,000 pulses at 7 V, 5 ms) (Methods), not only did device 1 show a significant conductance increase (by ~900%) (Fig. 5c), but Li⁺ ions also accumulated under electrode B. As a result, in configuration II, the same 500 stimulation pulses (6 V, 1 ms) can now produce a significant potentiation effect in device 2, where an increase in conductance by ~100% was observed (red curve in Fig. 5b). These results illustrate that potentiation in one device (device 1) can provide the critical ingredient (Li+ ions in this case) for nearby device 2, thus enabling synaptic potentiation in device 2.

We further studied a network consisting of four Li, MoS2-based synaptic devices sharing an electrode (Fig. 5d), and show that programming of targeted devices in the network can cooperatively affect the plasticity of neighbouring, non-targeted devices through ionic coupling effects. The network was initialized first to ensure that Li⁺ ions under the common electrode G were removed and accumulated near electrodes A, B, C and D (Methods; Fig. 5e). When an electric field was applied to drive Li⁺ ions from electrode A to replenish the removed Li⁺ ions under electrode G (Fig. 5f), the conductance of not only device 1, but also that of devices 2, 3 and 4, was increased (Fig. 5g,h). Moreover, stimulating device 1 to induce synaptic potentiation/depression (conductance increase/ decrease) (Fig. 5g) correspondingly led to the same type of synaptic plasticity effects in the other, non-stimulated devices (Fig. 5h), emulating synaptic cooperation behaviours in the network. Similar effects were also observed in devices 1, 3 and 4, when only device 2 was stimulated (Supplementary Fig. 22). Furthermore, the weight of the non-stimulated device (for example, device 4) was also substantially improved in a cumulative fashion, as more Li⁺ ions were accumulated under electrode G in a sequential fashion through the potentiation of devices 1, 2 and 3 (Fig. 5i-k). These results again verify that effective ionic coupling can be obtained among networks of memristive devices through in-plane Li+ ion exchange in the Li_xMoS₂ film.

The above results suggest that the ${\rm Li_x MoS_2}$ memristive system (or systems based on similar principles) can be used to faithfully emulate synaptic interaction effects in artificial neural networks. Looking into the future, continued device performance optimizations in terms of on/off ratio, power consumption, endurance and stability as well as device integration density are necessary to allow reliable implementation of more complex network systems. Possible strategies include optimization of the amount of intercalated Li⁺ ions (Supplementary Fig. 10), the number of layers in the ${\rm MoS_2}$ film (Supplementary Fig. 23), the length of the ${\rm MoS_2}$ film between the electrodes (Supplementary Fig. 24), the bias conditions (Supplementary Fig. 25), the device encapsulation techniques (Supplementary Fig. 26) and the device size (for example, down to ~100 nm or smaller) (Supplementary Fig. 27; see Supplementary Note 1 for further discussions).

In this study, we focused on memristive effects induced by structural phase transitions, as the initial Li+ ion concentration in all devices used in our study was higher than the critical value ($x \approx 0.28$) required for the 2H-1T' phase transition²¹ (Supplementary Fig. 4). We note that the intercalated Li+ ions can also lead to electron doping effects, as recently observed in 1T-TaS, films40 and ion-gated WSe₂ (ref. 41) synaptic transistors, as well as inducing strain in the MoS₂ film that causes band structure changes^{42,43}. These effects cannot be fully excluded in our devices and would require additional analysis. Nevertheless, compared with conventional memristive devices based on defect doping^{41,44,45} and filamentary formation⁴⁶⁻⁴⁹, the Li⁺ ion-induced memristive effects in 2D TMD films could offer advantages of better controllability and lower device variation and power consumption, and allow local, direct ionic coupling among synaptic devices in a network (see Supplementary Note 2 for further discussions).

In conclusion, we report reversible modulation of layered MoS_2 films through electric field-driven Li^+ ion redistribution, consistent with reversible and local 2H (semiconducting)–1T' (metallic) phase transition effects. The ionic modulation leads to reliable memristive behaviours in MoS_2 -based synaptic devices. The high in-plane diffusivity of Li^+ ions in turn allows efficient ionic coupling of multiple MoS_2 devices, and provides a mechanism to implement synaptic competition and synaptic cooperation effects in bio-inspired artificial neural networks. Similar strategies, based on controlled ionic modulation and ionic coupling processes, can be applied to other 2D TMD materials and used to develop future electronic devices and circuits, as well as to implement neuromorphic systems in a biorealistic fashion.

Online content

Any methods, additional references, Nature Research reporting summaries, source data, statements of data availability and associated accession codes are available at https://doi.org/10.1038/s41563-018-0248-5.

Received: 5 March 2018; Accepted: 13 November 2018; Published online: 17 December 2018

References

- Fiori, G. et al. Electronics based on two-dimensional materials. Nat. Nanotech. 9, 768–779 (2014).
- Mak, K. F. & Shan, J. Photonics and optoelectronics of 2D semiconductor transition metal dichalcogenides. *Nat. Photon.* 10, 216–226 (2016).
- 3. Schaibley, J. R. et al. Valleytronics in 2D materials. *Nat. Rev. Mater.* 1, 16055 (2016).
- Hong, J. et al. Layer-dependent anisotropic electronic structure of freestanding quasi-two-dimensional MoS₂. Phys. Rev. B 93, 075440 (2016).
- Gong, C. et al. Electronic and optoelectronic applications based on 2D novel anisotropic transition metal dichalcogenides. Adv. Sci. 4, 1700231 (2017).
- Jung, Y., Zhou, Y. & Cha, J. J. Intercalation in two-dimensional transition metal chalcogenides. *Inorg. Chem. Front.* 3, 452–463 (2016).

- Voiry, D., Mohite, A. & Chhowalla, M. Phase engineering of transition metal dichalcogenides. Chem. Soc. Rev. 44, 2702–2712 (2015).
- Wang, L., Xu, Z., Wang, W. & Bai, X. Atomic mechanism of dynamic electrochemical lithiation processes of MoS₂ nanosheets. *J. Am. Chem. Soc.* 136, 6693–6697 (2014).
- Chhowalla, M. et al. The chemistry of two-dimensional layered transition metal dichalcogenide nanosheets. *Nat. Chem.* 5, 263–275 (2013).
- Sun, X., Wang, Z., Li, Z. & Fu, Y. Q. Origin of structural transformation in mono- and bi-layered molybdenum disulfide. Sci. Rep. 6, 26666 (2016).
- Kappera, R. et al. Phase-engineered low-resistance contacts for ultrathin MoS₂ transistors. Nat. Mater. 13, 1128–1134 (2014).
- Cho, S. et al. Phase patterning for ohmic homojunction contact in MoTe₂. Science 349, 625–628 (2015).
- Lin, Y.-C., Dumcenco, D. O., Huang, Y.-S. & Suenaga, K. Atomic mechanism of the semiconducting-to-metallic phase transition in single-layered MoS₂. Nat. Nanotech. 9, 391–396 (2014).
- 14. Yang, H., Kim, S. W., Chhowalla, M. & Lee, Y. H. Structural and quantum-state phase transitions in van der Waals layered materials. *Nat. Phys.* 13, 931–937 (2017).
- Choe, D.-H., Sung, H.-J. & Chang, K. J. Understanding topological phase transition in monolayer transition metal dichalcogenides. *Phys. Rev. B* 93, 125109 (2016).
- Wang, Y. et al. Structural phase transition in monolayer MoTe₂ driven by electrostatic doping. Nature 550, 487–491 (2017).
- Ma, Y. et al. Reversible semiconducting-to-metallic phase transition in chemical vapor deposition grown monolayer WSe₂ and applications for devices. ACS Nano 9, 7383–7391 (2015).
- 18. Stephenson, T., Li, Z., Olsen, B. & Mitlin, D. Lithium ion battery applications of molybdenum disulfide (MoS₂) nanocomposites. *Energy Environ. Sci.* **7**, 209–231 (2014).
- Xu, X., Liu, W., Kim, Y. & Cho, J. Nanostructured transition metal sulfides for lithium ion batteries: progress and challenges. *Nano Today* 9, 604–630 (2014).
- Li, Y., Wu, D., Zhou, Z., Cabrera, C. R. & Chen, Z. Enhanced Li adsorption and diffusion on MoS₂ zigzag nanoribbons by edge effects: a computational study. J. Phys. Chem. Lett. 3, 2221–2227 (2012).
- Wang, H. et al. Electrochemical tuning of vertically aligned MoS₂ nanofilms and its application in improving hydrogen evolution reaction. *Proc. Natl Acad. Sci. USA* 110, 19701–19706 (2013).
- Xia, J. et al. Phase evolution of lithium intercalation dynamics in 2H-MoS₂. Nanoscale 9, 7533–7540 (2017).
- Xiong, F. et al. Li Intercalation in MoS₂: in situ observation of its dynamics and tuning optical and electrical properties. Nano Lett. 15, 6777–6784 (2015).
- Leng, K. et al. Phase restructuring in transition metal dichalcogenides for highly stable energy storage. ACS Nano 10, 9208–9215 (2016).
- Jo, S. H. et al. Nanoscale memristor device as synapse in neuromorphic systems. Nano Lett. 10, 1297–1301 (2010).
- Du, G. et al. Superior stability and high capacity of restacked molybdenum disulfide as anode material for lithium ion batteries. *Chem. Commun.* 46, 1106–1108 (2010).
- 27. Melitz, W., Shen, J., Kummel, A. C. & Lee, S. Kelvin probe force microscopy and its application. Surf. Sci. Rep. 66, 1–27 (2011).
- Wang, F. et al. Chemical distribution and bonding of lithium in intercalated graphite: identification with optimized electron energy loss spectroscopy. ACS Nano 5, 1190–1197 (2011).
- Rasamani, K. D., Alimohammadi, F. & Sun, Y. Interlayer-expanded MoS₂. Mater. Today 20, 83–91 (2017).
- Valov, I. et al. Nanobatteries in redox-based resistive switches require extension of memristor theory. Nat. Commun. 4, 1771 (2013).
- 31. Park, G.-S. et al. *In situ* observation of filamentary conducting channels in an asymmetric ${\rm Ta_2O_{5-x}/TaO_{2-x}}$ bilayer structure. *Nat. Commun.* **4**, 2382 (2013).
- Yang, Y. et al. Observation of conducting filament growth in nanoscale resistive memories. *Nat. Commun.* 3, 732 (2012).
- 33. Fonseca, R. in *Synaptic Tagging and Capture* (ed. Sajikumar, S.) 29–44 (Springer, New York, 2015).

- Muller, D., Hefft, S. & Figurov, A. Heterosynaptic interactions between UP and LTD in CA1 hippocampal slices. *Neuron* 14, 599–605 (1995).
- 35. Nishiyama, M., Hong, K., Mikoshiba, K., Poo, M.-M. & Kato, K. Calcium stores regulate the polarity and input specificity of synaptic modification. *Nature* **408**, 584–588 (2000).
- Royer, S. & Paré, D. Conservation of total synaptic weight through balanced synaptic depression and potentiation. *Nature* 422, 518–522 (2003).
- Bailey, C. H., Giustetto, M., Huang, Y.-Y., Hawkins, R. D. & Kandel, E. R. Is heterosynaptic modulation essential for stabilizing hebbian plasticity and memory. *Nat. Rev. Neurosci.* 1, 11–20 (2000).
- Sheridan, P. M. et al. Sparse coding with memristor networks. Nat. Nanotech. 12, 784–789 (2017).
- Borghetti, J. et al. 'Memristive' switches enable 'stateful' logic operations via material implication. *Nature* 464, 873–876 (2010).
- Yu, Y. et al. Gate-tunable phase transitions in thin flakes of 1T-TaS₂. Nat. Nanotech. 10, 270–276 (2015).
- Zhu, J. et al. Ion gated synaptic transistors based on 2D van der Waals crystals with tunable diffusive dynamics. Adv. Mater. 30, 1800195 (2018).
- He, K., Poole, C., Mak, K. F. & Shan, J. Experimental demonstration of continuous electronic structure tuning via strain in atomically thin MoS₂. Nano Lett. 13, 2931–2936 (2013).
- Conley, H. J. et al. Bandgap engineering of strained monolayer and bilayer MoS₂. Nano Lett. 13, 3626–3630 (2013).
- Sangwan, V. K. et al. Multi-terminal memtransistors from polycrystalline monolayer molybdenum disulfide. *Nature* 554, 500 (2018).
- Zhu, L. Q., Wan, C. J., Guo, L. Q., Shi, Y. & Wan, Q. Artificial synapse network on inorganic proton conductor for neuromorphic systems. *Nat. Commun.* 5, 3158 (2014).
- Yang, Y., Chen, B. & Lu, D. W. Memristive physically evolving networks enabling the emulation of heterosynaptic plasticity. *Adv. Mater.* 27, 7720–7727 (2015).
- Wang, Z. et al. Memristors with diffusive dynamics as synaptic emulators for neuromorphic computing. Nat. Mater. 16, 101–108 (2016).
- Zhu, X., Lee, J. & Lu, D. W. Iodine vacancy redistribution in organic– inorganic halide perovskite films and resistive switching effects. *Adv. Mater.* 29, 1700527 (2017).
- Zhu, X., Du, C., Jeong, Y. & Lu, D. W. Emulation of synaptic metaplasticity in memristors. *Nanoscale* 9, 45–51 (2017).

Acknowledgements

The authors thank K. Sun and A. Hunter for their help with the TEM measurements, and W. Ma, S. Lee, Q. Cui, J. Guo and Y. Li for helpful discussions and their assistance during the experiments. This work was supported in part by the National Science Foundation through grant numbers ECCS-1708700 and CCF-1617315.

Author contributions

X.Z. and W.D.L. designed the project and constructed the research frame. X.Z. and D.L. fabricated the devices and performed the measurements. X.Z., X.L. and W.D.L. analysed the experimental data. W.D.L directed the project. All authors discussed the results and implications and commented on the manuscript at all stages.

Competing interests

The authors declare no competing interests.

Additional information

Supplementary information is available for this paper at https://doi.org/10.1038/s41563-018-0248-5.

Reprints and permissions information is available at www.nature.com/reprints.

Correspondence and requests for materials should be addressed to W.D.L.

Publisher's note: Springer Nature remains neutral with regard to jurisdictional claims in published maps and institutional affiliations.

© The Author(s), under exclusive licence to Springer Nature Limited 2018

Methods

Device fabrication. Mechanically exfoliated MoS, flakes (3-80 nm thick) were transferred to a SiO₂/Si substrate with 300-nm-thick thermally oxidized SiO₂. Gold electrodes were patterned on the flakes by photolithography followed by electron-beam evaporation of Au metal (100 nm thick) and lift-off processes. To create the transparent Au/ITO electrodes, an ITO film (50 nm thick) was deposited on a thin Au film (5 nm thick) by sputtering using an ITO ceramic target, followed by annealing at 200 °C for 1 h. The network device structure shown in Fig. 5d was obtained by patterning a MoS₂ flake through photolithography and chemical dry-etching using XeF₂ as the reactant and the patterned photoresist as the mask. The XeF₂ pressure during etching was fixed at 3 torr and the etching process lasted for 60 s. The sample was then immersed in acetone (≥99%, Sigma Aldrich) for 12h followed by an oxygen plasma treatment (60 °C, 100 W, 20 s) to remove the photoresists and surface residues. Afterwards, Au electrodes (100 nm) were patterned by photolithography, followed by electron-beam evaporation and lift-off processes. To intercalate Li+ ions to the as-fabricated devices, the samples were immersed in 3 ml 1.6 M n-butyl lithium solution (Sigma Aldrich) in a nitrogen glovebox at room temperature for 0.5 to 3h, depending on the desired degree of lithiation. The devices studied in Figs. 1-3 and 5 were lithiated for ~1.5-2 h while the devices studied in Fig. 4 were lithiated for ${\sim}1.2\,h.$ After lithiation, the devices were removed and rinsed with hexane (95%, Sigma Aldrich) to remove the residues of butyl lithium. The samples were then blow-dried by nitrogen gas. To encapsulate the devices, the samples were first transferred to a N2-filled glovebox, and glass lids were then used to cover the Li_xMoS₂ films (without covering the contact pads used to perform electrical measurements) and sealed by applying ultraviolet-cured epoxy.

XPS measurement. XPS characterizations were performed using a Kratos Axis Ultra system with a monochromated Al anode. The source was operated at 14 kV with an emission current of 8 mA.

Raman imaging. A Raman spectroscope (Renishaw StreamlineHR) equipped with a 532-nm laser was used to obtain the Raman spectra of the devices at a laser power of ~3 mW. A step size of ~300 nm was used to acquire the Raman maps.

Electrical characterization. Most of the measurements were performed in vacuum in a probe station (Desert Cryogenics TTP4) to minimize the effect of the moisture in air on device performance. The d.c. *I–V* and pulse measurements were performed using a Keithley 4200 semiconductor parameter analyser.

KPFM and AFM measurements. A scanning probe microscope (Dimension V, Icon, Bruker) was used to perform the KPFM and AFM measurements. For KPFM measurements, a tip coated with Pt/Ir thin film (SCM-PIC-V2, Bruker) was used in the amplitude modulation KPFM mode, and a small constant bias voltage ($\sim\!1$ V) was applied across the device. After acquiring the surface topography in the first scan, the tip was lifted up by $\sim\!70$ nm and scanned over the sample following the obtained topographical profile to collect the surface potential data. For AFM

measurements, the microscopy was performed in the standard tapping mode with the same tip used in the KPFM measurements.

TEM imaging and EELS measurements. Samples for TEM were prepared using an FEI Helios 450S dual-beam focused ion beam system. The samples were obtained in a region underneath electrode B, where the morphology was found to change reversibly under electric biases. A bias voltage of $4\,\mathrm{V}$ and $-4\,\mathrm{V}$ was applied to electrode B for $20\,\mathrm{min}$, respectively, to obtain samples at the HRS and LRS. HRTEM imaging was conducted in a Cs-corrected JEOL $3011~(300\,\mathrm{kV})$ transmission electron microscope. For the EELS measurement, a low electron-beam current of $10-20~\mathrm{pA}$ was used. The exposure time was $0.1~\mathrm{s}$.

Scanning electron microscopy imaging. Scanning electron micrographs of the devices were acquired from a Hitachi SU8000 system operated at $10\,\mathrm{kV}$ with an emission current of $7\,\mu\mathrm{A}$.

Initialization and conditioning processes for synaptic competition implementation. To initialize the two-device system shown in Fig. 4b, a positive voltage bias (4 V) was applied on both electrodes A and B for several minutes, with electrode G grounded. This process caused Li⁺ ions to accumulate under the common electrode G. A short lithiation time (~1.2 h) was used to prepare the samples used in this experiment to intentionally limit the total amount of available Li⁺ ions, as evidenced by a smaller thickness increase observed in Fig. 4b compared to samples obtained from longer lithiation times (such as that shown in Fig. 3a). To obtain configuration I in Fig. 4c, we first applied a negative bias voltage (-4V) on electrode A (with electrode G grounded), which drove Li⁺ ions towards electrode A. Afterwards, a bias voltage of -4V was applied on electrode B, which drove the remaining Li⁺ ions towards electrode B. To achieve configuration II in Fig. 4c, the biasing sequence was reversed, with a negative voltage bias applied on electrode B first, followed by the biasing of electrode A.

Initialization and conditioning processes for synaptic cooperation implementation. To initialize the two-device system in Fig. 5a, a negative voltage ($-5\,\mathrm{V}$) was applied on electrode A for several minutes with electrode C grounded, which programmed the system to configuration I. This process caused the Li⁺ ions in the system to accumulate under electrode A, as evidenced by the AFM height measurement shown in Fig. 5a. To achieve configuration II, starting from configuration I, 2,000 pulses (7 V, 5 ms) were applied on electrode A with electrode B grounded. This process drove Li⁺ ions under electrode A towards electrode B, as evidenced by the AFM height image for configuration II shown in Fig. 5a. To initialize the network system shown in Fig. 5e, negative bias voltages ($-4\,\mathrm{V}$) were applied on electrodes A, B, C and D with electrode G grounded, which depleted Li⁺ ions from the region under the common electrode G.

Data availability

The data that support the plots within this paper and other findings of this study are available from the corresponding author upon reasonable request.